RSC Advances

PAPER

View Article Online
View Journal | View Issue

Cite this: *RSC Adv.*, 2026, **16**, 25348

Investigations of heavy p-block elements (Sn, Sb, Bi) in 2-amino-5-methylpyridinium halogenometallate complexes: optical absorption and electrical properties

Mohamed Loucif,*[a] Iheb Garoui,[b] Souad Chkoundali,[b] Rima Mohammed Altalib,[c] Mehdi Akermi*[d] and Abderrazek Oueslati*[b]

The interaction between 2-amino-5-methylpyridinium and heavy p-block metal chlorides (Sn, Sb, and Bi) results in the formation of three hybrid compounds: $(C_6H_9N_2)_2SnCl_6$, $(C_6H_9N_2)_3[BiCl_6]$, and $(C_6H_9N_2)_2[Sb_2Cl_8]$. Their structural, optical, and electrical properties were systematically examined by powder X-ray diffraction, UV–visible spectroscopy, and complex impedance spectroscopy in order to elucidate the effect of metal-center substitution on their physical behavior. Optical analysis reveals a gradual narrowing of the band gap from Sb- to Bi-containing compounds. The estimated band gap energies are 3.49 eV for $(C_6H_9N_2)_2[Sb_2Cl_8]$, 3.36 eV for $(C_6H_9N_2)_2SnCl_6$, and 3.10 eV for $(C_6H_9N_2)_3[BiCl_6]$, indicating enhanced electronic delocalization with increasing atomic number. Electrical measurements demonstrate a negative temperature coefficient of resistance (NTCR) for all samples in the temperature range 343–383 K, confirming their semiconducting character. The DC conductivity exhibits thermally activated behavior consistent with the Arrhenius model. The calculated activation energies are 0.71 eV (Sb-based), 0.54 eV (Sn-based), and 0.40 eV (Bi-based). Although the Bi-containing compound shows the lowest activation energy, the overall conductivity decreases in the order $(C_6H_9N_2)_2[Sb_2Cl_8]$ > $(C_6H_9N_2)_2SnCl_6$ > $(C_6H_9N_2)_3[BiCl_6]$. These findings highlight that metal-ion substitution represents an effective approach to modulate the electronic structure and charge transport properties of 2-amino-5-methylpyridinium-based hybrid materials, underscoring their potential for semiconducting and electronic device applications.

Received 11th March 2026
Accepted 8th May 2026

DOI: 10.1039/d6ra02081j

rsc.li/rsc-advances

1. Introduction

The rapid development of functional materials for optoelectronic and electronic applications has intensified the search for alternatives to conventional inorganic semiconductors. In this context, hybrid organic–inorganic metal halides have emerged as a versatile materials family due to their structural adaptability and tunable electronic properties.[1] Unlike purely inorganic solids, hybrid systems allow the independent modification of the organic and inorganic components, enabling fine control over dimensionality, symmetry, band structure, and polarization behavior.[2,3]

Growing interest has recently focused on post-transition metal ions from the heavier p-block region because of their distinctive electronic configuration. Cations such as Sn^{2+}, Sb^{3+}, and Bi^{3+} possess filled s orbitals that can interact with surrounding anions in a non-uniform manner.[4–6] This interaction generates anisotropic electron density around the metal center, frequently resulting in deviations from ideal coordination geometries. Such structural irregularities can modify crystal symmetry, influence local dipole formation, and alter the distribution of electronic states near the band edges. Consequently, compounds incorporating these elements often exhibit pronounced structural adaptability together with distinctive optical and dielectric characteristics. Within metal–halide architectures, the fundamental electronic properties arise from the hybridization between the valence orbitals of the metal cation and the p orbitals of the halide ligands.[7] Variations in bond angles, bond lengths, and coordination distortions directly affect this hybridization, thereby tuning the band gap magnitude and carrier mobility. In general, Sn-based

[a]*Laboratory of Materials Chemistry and Applications, Faculty of Sciences and Technology, Tissemsilt University, Algeria. E-mail: loucif.mohamed@univ-tissemsilt.dz.fr*

[b]*Laboratory of Spectroscopic Characterization and Optical Materials, Faculty of Sciences, University of Sfax, B.P. 1171, 3000 Sfax, Tunisia. E-mail: oueslatiabderrazek@yahoo.fr*

[c]*Department of Physics, Faculty of Science, Elmergib University, Libya. E-mail: rmaltalib@elmergib.edu.ly*

[d]*Department of Physics Sciences, College of Science, Jazan University, P.O. Box. 114, Jazan 45142, Kingdom of Saudi Arabia. E-mail: makermi@jazanu.edu.sa*

halogenometallates tend to favor stronger orbital overlap, which can promote efficient charge transport and narrower energy gaps.[7,8] By contrast, Sb- and Bi-containing analogues are typically associated with greater chemical robustness and lower toxicity relative to conventional lead systems, positioning them as promising materials for environmentally benign optoelectronic applications.[9,10]

The organic cation plays a pivotal role in determining the structural organization and functional properties of hybrid materials. In particular, aromatic ammonium species such as substituted pyridinium derivatives strengthen the crystal architecture through a combination of hydrogen bonding and coulombic interactions with the inorganic framework.[11] These supramolecular forces govern the connectivity of the metal–halide units, enabling the formation of zero-, one-, or two-dimensional arrangements. Consequently, they influence lattice stiffness, structural stability, and dielectric response. The incorporation of polar organic groups further contributes to interfacial and dipolar polarization effects, which are especially pronounced in the low-frequency region. Beyond their structural contribution, pyridine-based compounds are of considerable importance in heterocyclic and medicinal chemistry. Their aromatic π-electron system, combined with the lone pair on the nitrogen atom, provides strong coordination ability and versatile hydrogen-bonding behavior.[12,13] Substituted pyridines are widely employed as ligands in coordination chemistry, as building blocks for supramolecular assemblies, and as key motifs in biologically active molecules. When integrated into organic–inorganic hybrid frameworks, these derivatives often enhance structural robustness, promote selective intermolecular recognition, and generate diverse packing motifs.

Among these compounds, 2-amino-5-methylpyridine (2A5MP) is particularly noteworthy due to the simultaneous presence of an amino group and a ring nitrogen donor site.[14] This dual functionality enables multiple coordination modes and flexible hydrogen-bonding patterns. The materials compiled in Table 1 reflect the structural richness associated with this organic moiety.

In each case, 2-amino-5-picoline acts as the organic component combined with different divalent metal cations and halide anions, giving rise to architectures ranging from isolated units to extended supramolecular networks. The dimensionality and physical characteristics of these frameworks are strongly modulated by the nature of the metal center and halide species. Notably, all reported structures incorporating 2-amino-5-methylpyridinium crystallize in centrosymmetric space groups, highlighting the adaptability of 2A5MP in assembling ordered hybrid systems. Altogether, these observations emphasize the potential of this ligand for designing multifunctional organic–inorganic materials with tunable structural and physicochemical properties. In this study, we explored centrosymmetric heavy p-block elements (Sn, Sb, and Bi) incorporated into 2-amino-5-methylpyridinium halogenometallate systems, namely $(C_6H_9N_2)_2SnCl_6$, $(C_6H_9N_2)_3BiCl_6$, and $(C_6H_9N_2)_2Sb_2Cl_8$. These materials were synthesized using a slow evaporation method, and their phase purity was verified by X-ray powder diffraction (XRPD). Employing the same organic cation in all three compounds provides a uniform supramolecular framework, allowing a direct evaluation of the influence of metal substitution (Sn^{4+}, Bi^{3+}, and Sb^{3+}) on crystal structure, electronic configuration, and electrical behavior. Optical absorption measurements carried out offered valuable information regarding electronic transitions and band gap energies. Furthermore, impedance spectroscopy was conducted to investigate dielectric relaxation processes related to point defects, interfacial polarization, and grain-boundary contributions.

The environmental and health concerns associated with lead-based perovskites have motivated the search for safer alternatives. Although Pb-halide perovskites show excellent optoelectronic properties, their toxicity limits practical applications. In this context, Sn-, Sb-, and Bi-based halide materials are emerging as promising lead-free candidates due to their lower toxicity and reduced environmental impact. In addition, Sb- and Bi-based compounds often exhibit improved chemical and thermal stability compared to lead-based systems, attributed to stronger metal–halide bonding and enhanced structural rigidity. These features provide better resistance to moisture and thermal degradation, making lead-free halide materials attractive for sustainable optoelectronic applications.[24,25]

This work explores the influence of heavy p-block elements (Sn, Sb, and Bi) on the structural, optical absorption, and electrical properties of 2-amino-5-methylpyridinium halogenometallate complexes. Particular attention is given to understanding how metal-ion substitution governs charge transport and dielectric behavior, with the aim of establishing structure–property relationships relevant to optoelectronic applications.

Table 1 Representative hybrid materials incorporating 2-amino-5-picoline, along with their chemical compositions, crystallographic systems, and corresponding space groups

Compound	System	Space group	Ref.
$(C_6H_9N_2)_2SnBr_6$	Monoclinic	$P2_1/c$	3
$(C_6H_9N_2)_3BiCl_6$	Triclinic	$P\bar{1}$	9
$(C_6H_9N_2)_2MnI_4$	Triclinic	$P\bar{1}$	15
$(C_6H_9N_2)_2CoCl_4$	Monoclinic	$P2_1/c$	16
$(C_6H_9N_2)_2MnBr_4$	Triclinic	$P\bar{1}$	17
$(C_6H_9N_2)_2CdCl_4$	Triclinic	$P\bar{1}$	18
$(C_6H_9N_2)FeCl_4$	Monoclinic	$P2_1/c$	19
$(C_6H_9N_2)_2[SbBr_4]Br$	Monoclinic	$C2/m$	20
$(C_6H_9N_2)_2Sb_2Cl_8$	Triclinic	$P\bar{1}$	21
$(C_6H_9N_2)_2SnCl_6$	Monoclinic	$P2_1/c$	22
$(C_6H_9N_2)_2ZnCl_4$	Monoclinic	$P2_1/c$	23

2. Experimental procedures

2.1. Materials and reagents

All chemicals used in this study were of analytical grade and were utilized directly without additional purification. Antimony(III) chloride ($SbCl_3$, 99.95%), bismuth(III) chloride ($BiCl_3$, 99.9%), and tin(II) chloride dihydrate ($SnCl_2{,}2H_2O$, 99.9%) were obtained from Sigma-Aldrich. The organic ligand, 2-amino-5-methylpyridine ($C_6H_8N_2$, 98%), was also sourced from Sigma-Aldrich, while concentrated hydrochloric acid (37%) was

Fig. 1 Crystals of (a) $(C_6H_9N_2)_2[Sb_2Cl_8]$, (b) $(C_6H_9N_2)_2SnCl_6$ and (c) $(C_6H_9N_2)_3[BiCl_6]$.

supplied by FLUKA. Freshly distilled water was used for all solution preparations and crystallizations to ensure reproducible crystal formation and to reduce the presence of extraneous ions. All synthetic and characterization procedures were carried out under standard laboratory conditions at temperatures ranging from 25 to 30 °C.

2.2. Synthesis of compounds by slow evaporation method

The three hybrid systems $(C_6H_9N_2)_2SnCl_6$, $(C_6H_9N_2)_3[BiCl_6]$, and $(C_6H_9N_2)_2[Sb_2Cl_8]$ were prepared following literature procedures using the slow evaporation technique.[9,21,22] In this method, the precursors are dissolved in an appropriate solvent, and the solution is left undisturbed at room temperature. Gradual evaporation of the solvent induces supersaturation, promoting the growth of well-defined single crystals. This approach provides control over crystal size and morphology and is particularly suitable for producing crystals for structural and spectroscopic analysis.[26,27]

2.2.1. Preparation of $(C_6H_9N_2)_3[BiCl_6]$. 0.1 g of 2-amino-5-picoline ($C_6H_8N_2$) and 0.0972 g of bismuth(III) chloride ($BiCl_3$) were dissolved in a small amount of distilled water. To this solution, 0.75 mL of concentrated hydrochloric acid (HCl, 37%) was added. The mixture was left to stand at room temperature (~28 °C). As the solvent slowly evaporated, white crystals of millimeter-scale dimensions were obtained.

2.2.2. Preparation of $(C_6H_9N_2)_2[Sb_2Cl_8]$. 0.108 g of 2-amino-5-picoline ($C_6H_8N_2$), 0.228 g of antimony(III) chloride ($SbCl_3$), and 0.036 g of hydrochloric acid (HCl) were dissolved in a small volume of distilled water. The solution was allowed to stand at room temperature (~28 °C). With slow solvent evaporation, well-formed, colorless crystals were obtained.

2.2.3. Preparation of $(C_6H_9N_2)_2SnCl_6$. The organic precursor 2-amino-5-picoline (0.0959 g) was reacted with $SnCl_4$, generated *in situ* from tin(II) chloride dihydrate ($SnCl_2$, $2H_2O$; 0.1 g) in hydrochloric acid. The solution was left undisturbed at room temperature, and after seven days of slow evaporation, millimeter-sized white crystals of $(C_6H_9N_2)_2SnCl_6$ were formed.

Fig. 1 illustrates the obtained 2-amino-5-methylpyridine-based crystals. All crystals were collected by filtration, rinsed with distilled water, and air-dried prior to further characterization.

2.3. Experimental characterization

Powder X-ray diffraction (PXRD) analysis of the synthesized compound was carried out at room temperature (298 K) using a Bruker D8 Advance diffractometer. The measurements were performed with Cu Kα radiation ($\lambda = 1.5406$ Å) over a 2θ interval from 5° to 50°, employing a step increment of 0.02°.

The UV–visible absorption spectra were recorded at ambient temperature using a Shimadzu 3101 PC spectrophotometer equipped with a double-beam monochromator. Measurements were carried out over the wavelength range of 200–800 nm. This technique enables evaluation of the absorbance (A), identification of electronic transitions, and estimation of the

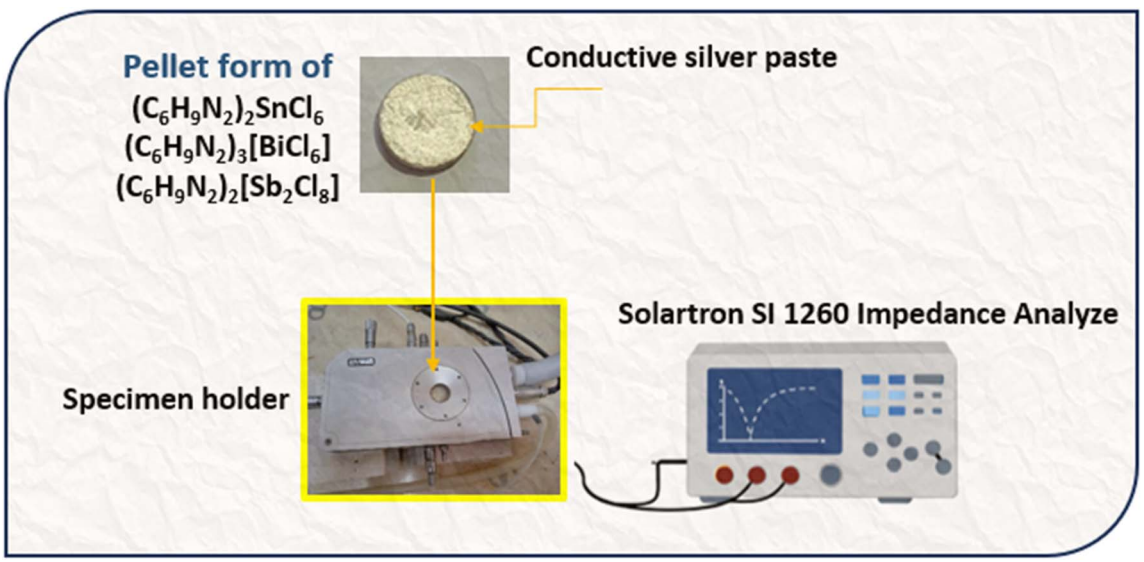

Fig. 2 Schematic illustration along with the sample geometry for CIS measurement.

corresponding optical band gap energies of the 2-amino-5-methylpyridine-based samples.

The electrical response of the samples was investigated using impedance spectroscopy (IS) with a Solartron SI-1260 frequency response analyzer coupled to a programmable heating system. For this purpose, the crystals were ground into a fine powder and then pressed into pellets with a diameter of 8 mm and a thickness of 1 mm. Both faces of each pellet were coated with a thin layer of silver paste to ensure good electrical contact. The relative density of the pellets was determined using the geometrical method based on their measured mass and dimensions. The pellet volume was calculated using $V = \pi r^2 h$, yielding $V = 0.0503$ cm^3. Using a measured mass of approximately 0.26 g, the experimental density was determined from $\rho_{exp} = m\ V^{-1}$,[28] giving a value of about 5.17 g cm^{-3}. The temperature control system provided a resolution of 0.1 K and maintained stability within ±0.5 K during the measurements. Impedance spectra were recorded over a frequency range of 20 Hz to 1 MHz and within a temperature interval of 343–383 K. This experimental configuration enabled a detailed investigation of the charge transport mechanism and the negative temperature coefficient of resistance (NTCR) behavior. The impedance measurement setup is shown in Fig. 2.

3. Results and discussion

3.1. Crystal structure of the three samples: a brief overview

The crystallographic information for all investigated structures has been deposited at the Cambridge Crystallographic Data Centre (CCDC) under the following deposition numbers: 2225545 for $(C_6H_9N_2)_2[Sb_2Cl_8]$,[21] 2366479 for $(C_6H_9N_2)_3[BiCl_6]$,[9] and 2231670 for $(C_6H_9N_2)_2SnCl_6$.[22] The corresponding crystal packing diagrams are presented in Fig. 3.

The overall stability and cohesion of these hybrid materials are ensured by a network of N–H···Cl hydrogen bonds linking the protonated organic cations to the inorganic anionic units. A comparison of the crystal symmetries shows that the Bi- and Sb-based compounds adopt a triclinic structure (P1), whereas the Sn-based compound crystallizes in the monoclinic system ($P2_1/c$). This distinction can be explained by the presence of

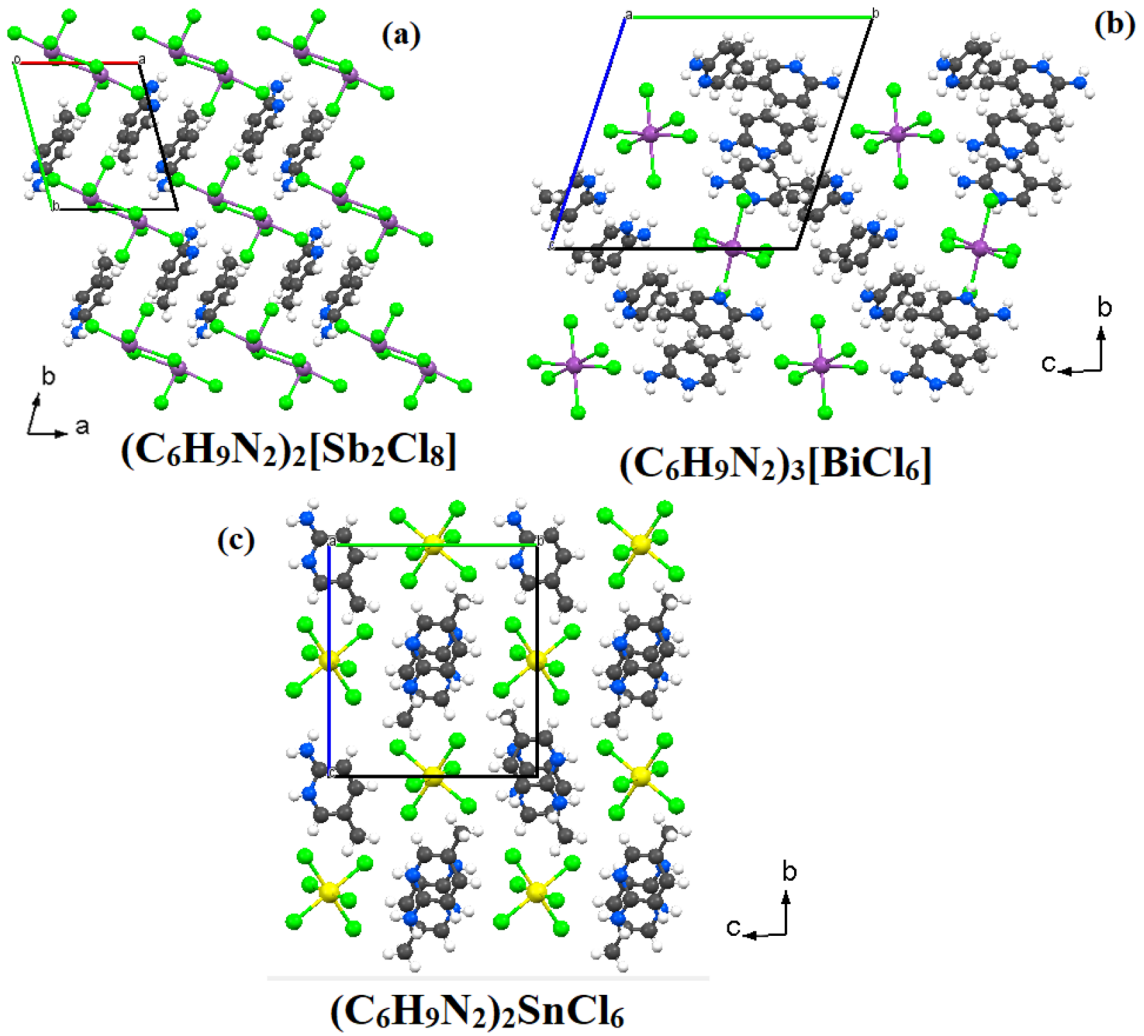

Fig. 3 Structural projections of (a) $(C_6H_9N_2)_2[Sb_2Cl_8]$ and (b) $(C_6H_9N_2)_3[BiCl_6]$ along the crystallographic *c*-axis, and (c) $(C_6H_9N_2)_2SnCl_6$ along the crystallographic *a*-axis.

a stereochemically active ns^2 lone pair in Bi^{3+} and Sb^{3+} cations ($6s^2$ and $5s^2$, respectively).[29,30] The asymmetric electron density associated with these lone pairs induces pronounced distortions in the coordination polyhedra, leading to irregular $[BiCl_6]^{3-}$ and $[Sb_2Cl_8]^{2-}$ units and consequently favoring a low-symmetry triclinic arrangement. In contrast, the Sn^{4+} ion does not exhibit a stereochemically active lone pair, allowing the formation of more regular $[SnCl_6]^{2-}$ octahedra. This higher degree of geometrical symmetry promotes a more ordered crystal packing and results in a monoclinic structure. Moreover, the hydrogen-bonding scheme reflects these structural differences: it is more disordered and anisotropic in the Bi and Sb compounds, supporting the triclinic symmetry, while in the Sn compound it becomes more homogeneous, contributing to the stabilization of the monoclinic phase. Such structural behavior is in line with the widely recognized influence of ns^2 lone pairs in generating distortions within p-block metal halide frameworks. These structural characteristics have a direct impact on the physical properties of the materials. In particular, the distortions and asymmetry observed in the Bi- and Sb-based compounds are closely linked to changes in their electronic structure and charge transport mechanisms. In contrast, the more symmetric Sn-based framework leads to a distinct optical behavior and a different trend in electrical conductivity.

3.2. Powder X-ray diffraction (PXRD) analysis

To evaluate the influence of the 2-amino-5-methylpyridine organic moiety on the crystal architecture of $(C_6H_9N_2)_2SnCl_6$, $(C_6H_9N_2)_3[BiCl_6]$, and $(C_6H_9N_2)_2[Sb_2Cl_8]$, powder X-ray diffraction measurements were performed at ambient temperature. The diffraction patterns were analyzed by Rietveld refinement profiles using the FullProf program,[31] and the corresponding refinement profiles are presented in Fig. 4(a–c). The extracted crystallographic parameters are compiled in Table 2 and show good consistency with previously reported data.[9,21,22]

Table 2 Crystallographic parameters obtained from Rietveld profiles refinement

Formula	$(C_6H_9N_2)_2SnCl_6$	$(C_6H_9N_2)_2[Sb_2Cl_8]$	$(C_6H_9N_2)_3[BiCl_6]$
Crystal system	Monoclinic	Triclinic	Triclinic
Space group	$P2_1/c$	$P\bar{1}$	$P\bar{1}$
Lattice parameters			
a (Å)	7.689	7.981	14.363
b (Å)	10.768	9.088	14.405
c (Å)	12.091	9.371	14.417
α (°)	90	86.357	104.544
β (°)	96.294	69.174	104.440
γ (°)	90	74.860	100.584
Refinement parameters			
R_{exp} (%)/R_p (%)/R_{wp} (%)	19.62/15.9/21	10.6/27.6/17.3	10.9/14.6/19.4
GOF (χ^2)	1.14	2.67	3.18

3.3. Investigation of optical properties and band gap energy

3.3.1. UV–vis absorption analysis. Ultraviolet–visible (UV–vis) spectroscopy is widely employed to probe the optical response of materials, determine key optical constants, and explore the electronic band structure of semiconductors.[32] The absorption process arises from the interaction between incident photons and the electronic states of the material, providing valuable information about its electronic transitions. In this work, the optical properties of the three hybrid compounds were examined using UV–vis spectroscopy (Fig. 5).

The absorption spectra of $(C_6H_9N_2)_2[Sb_2Cl_8]$, $(C_6H_9N_2)_3[BiCl_6]$ and $(C_6H_9N_2)_2SnCl_6$, measured over the 200–800 nm wavelength range, exhibit comparable overall features. All samples show strong absorption in the ultraviolet region followed by a sharp decline in intensity toward the visible region. Distinct absorption bands are observed between approximately 280 and 360 nm, which are mainly associated with ligand-to-metal charge transfer ($Cl^- \rightarrow M$) transitions within the inorganic octahedral units,[3,5,9,21,22,33] in addition to possible π–π^* transitions related to the organic moieties.[3,16] A clear difference appears in the position of the absorption edges depending on the metal center. The Sb-containing compound absorbs at shorter wavelengths, indicating a comparatively larger band gap. In contrast, the Bi-based material displays a red-shifted absorption band around 355 nm, suggesting a reduced band gap energy. The Sn analogue shows intermediate behavior between the Sb and Bi systems. Above 400 nm, the absorption intensity becomes very low for all compounds, confirming their wide band gap semiconducting nature and weak response in the visible region. The progressive shift of the

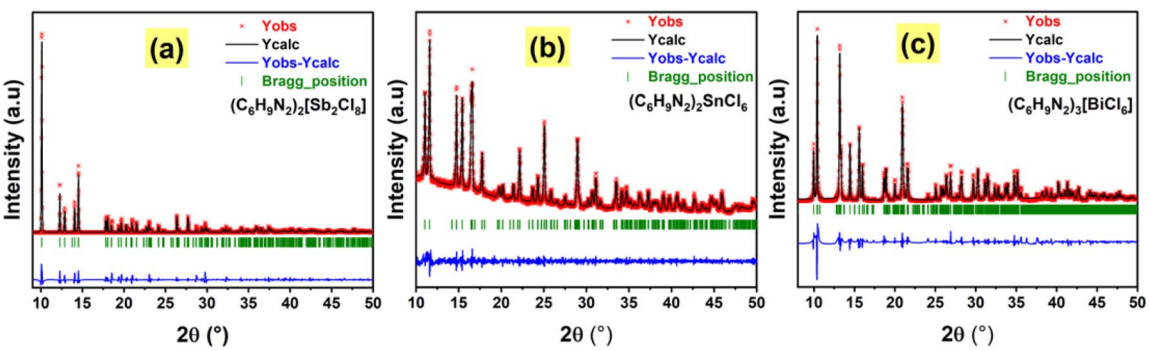

Fig. 4 XRD patterns of 2-amino-5-methylpyridine-based samples: (a) $(C_6H_9N_2)_2[Sb_2Cl_8]$, (b) $(C_6H_9N_2)_2SnCl_6$ and (c) $(C_6H_9N_2)_3[BiCl_6]$.

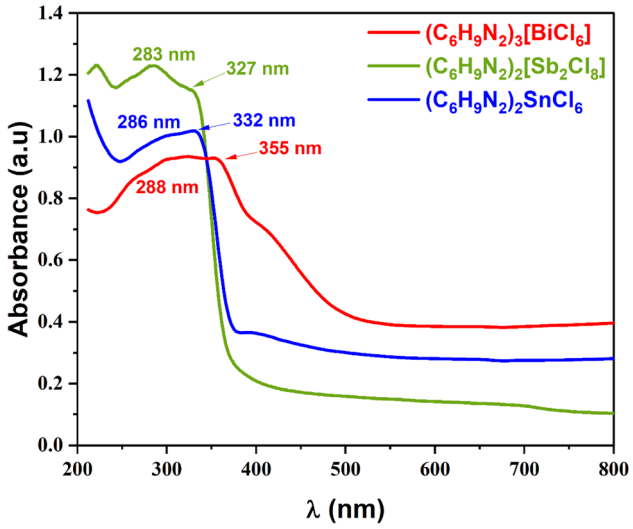

Fig. 5 UV–visible absorption spectra of the of 2-amino-5-methylpyridine-based samples.

absorption edge from Sb to Bi highlights the significant role of the metal ion, particularly the influence of its atomic size, electronic structure, and stereochemically active lone-pair electrons on the electronic properties of the halogenometallate framework.

3.3.2. Band gap determination (Tauc plot). The optical band gap values were evaluated using the Tauc formalism, derived from the absorption edge behavior,[34] according to the following expression:

$$(\alpha h\nu)^2 = P(h\nu - E_g) \quad (1)$$

where "P" is a proportionality constant, "E_g" denotes the optical band gap energy, and "α" represents the absorption coefficient. The latter was calculated from the measured absorbance using:

$$\alpha = \frac{2.303\ A}{d} \quad (2)$$

In which "A" is the absorbance and "d" corresponding to the sample thickness.

To determine the band gap energies, plots of $(\alpha h\nu)^2$ *versus* photon energy $h\nu$ were constructed. Fig. 6(a–c) shows the variation of $(\alpha h\nu)^2$ as a function of photon energy $(h\nu)$ for the three synthesized compounds. The linear portion near the absorption edge was extrapolated to intersect the energy axis at $(\alpha h\nu)^2 = 0$. The intercept of this linear fit provides the value of E_g, indicating direct allowed electronic transitions for all compounds, in agreement with the reported literature.[3,21,22] The estimated band gap energies are 3.49 eV for $(C_6H_9N_2)_2[Sb_2Cl_8]$, 3.36 eV for $(C_6H_9N_2)_2SnCl_6$, and 3.10 eV for $(C_6H_9N_2)_3[BiCl_6]$. These values

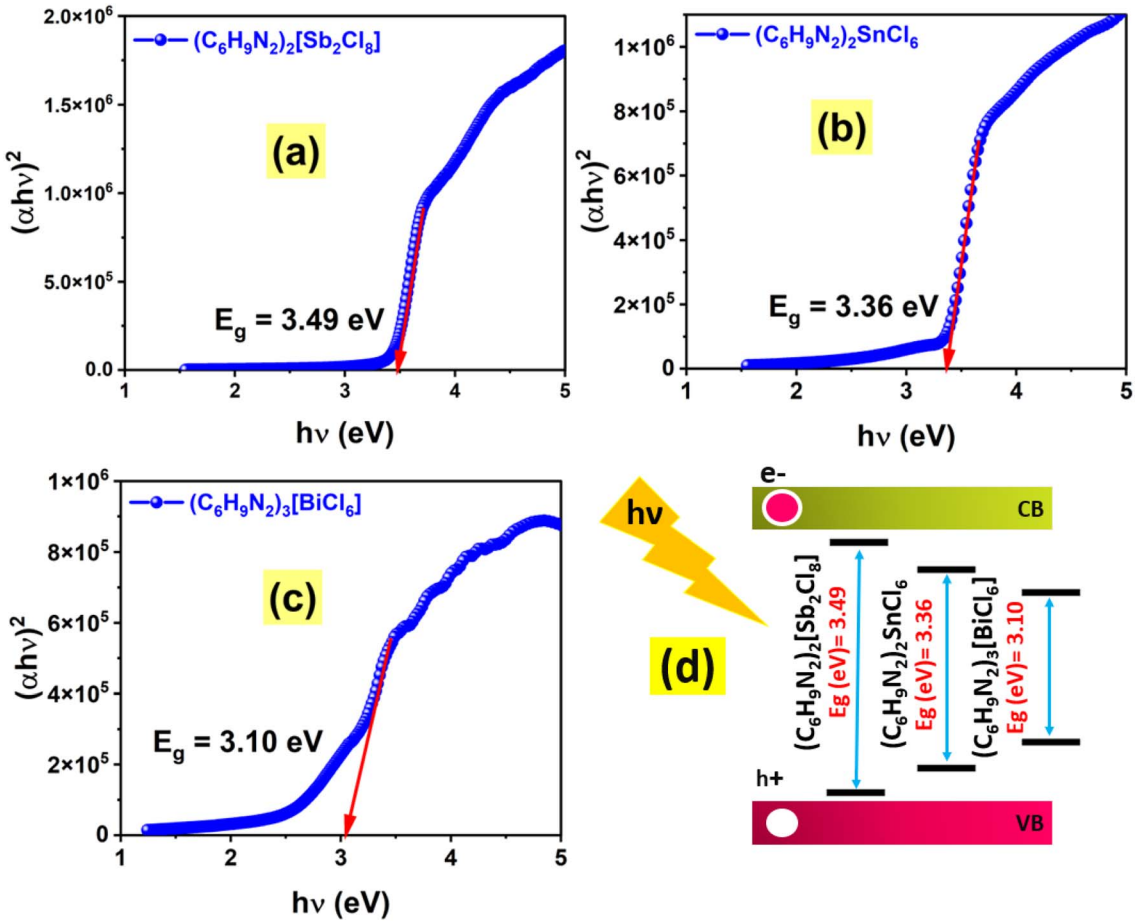

Fig. 6 Tauc plots of 2-amino-5-methylpyridinium-based compounds: (a) $(C_6H_9N_2)_2[Sb_2Cl_8]$, (b) $(C_6H_9N_2)_2SnCl_6$, (c) $(C_6H_9N_2)_3[BiCl_6]$ and (d) schematic illustration of the optical absorption process showing a progressive decrease in band gap energy from Sb-to Bi-based compounds.

Table 3 Gap energy values (E_g) reported for (Sn, Sb, Bi)-based organic–inorganic hybrid materials

Compounds	Gap energy: E_g (eV)	References
$(C_6H_9N_2)_2[Sb_2Cl_8]$	3.49	This work
$(C_6H_9N_2)_2SnCl_6$	3.36	This work
$(C_6H_9N_2)_3[BiCl_6]$	3.10	This work
$(CH_3NH_3)_2SnBr_6$	3.21	32
$(C_2H_8N)_3BiBr_6$	2.84	37
$(C_9H_{14}N)_3BiCl_6$	3.40	38
$[C_3H_5N_2S]SbCl_4$	3.54	39
$(C_6H_9N_2)_2[SbBr_4]Br$	3.05	20
$(C_8H_{12}N)_2[SnCl_6]$	4.11	40

confirm the wide band gap semiconducting character of the three materials.

A progressive reduction in the optical band gap is observed following the order: E_g(Sb) > E_g(Sn) > E_g(Bi). The decrease from (Sb) to (Bi) can be attributed to the enlargement of the atomic size[35] (Fig. 6(d)), the increasing strength of spin–orbit coupling, and the more pronounced effect of the stereochemically active ns^2 lone-pair electrons in the heavier metal centers. Notably, the Bi-containing compound shows the greatest band gap narrowing, which can be associated with stronger metal–halide orbital overlap and enhanced relativistic effects within the inorganic framework.[36] Overall, the Tauc analysis highlights the crucial role of the metal center in modulating the electronic structure and optical performance of these hybrid halogenometallate systems.

A comparison with previously reported studies reveals that the measured band gap values align well with those of related hybrid halide materials. Table 3 presents the band gap energy (E_g) values reported for Sn-, Sb-, and Bi-based organic–inorganic hybrid materials.

For instance, compounds such as $(CH_3NH_3)_2SnBr_6$ (3.21 eV)[32] and $(C_9H_{14}N)_3BiCl_6$ (3.40 eV)[38] show similar energy gaps, further confirming the semiconducting behavior of this class of materials. On the other hand, higher band gap values, such as that observed for $(C_8H_{12}N)_2[SnCl_6]$ (4.11 eV),[40] can be linked to differences in structural arrangement, as well as the size and chemical nature of the organic cations and halide ions. The variation in E_g can be mainly attributed to several factors. First, the type of halide plays a crucial role, with chloride-containing compounds typically exhibiting larger band gaps than bromide analogues due to their higher electronegativity and weaker orbital interactions. Second, the nature of the metal center influences the electronic band structure, since the electronic configurations of Sb^{3+}, Sn^{4+}, and Bi^{3+} determine the positions of the valence and conduction bands. Finally, structural aspects such as octahedral distortion and the degree of connectivity within the inorganic framework also impact band dispersion. Overall, these findings indicate that the investigated materials belong to the category of wide-band-gap semiconductors, making them more appropriate for insulating or ultraviolet applications.

3.3.3. Evaluation of the Urbach energy (E_u) in 2-amino-5-methylpyridinium halometallates. The Urbach energy (E_u) was evaluated to gain insight into the extent of structural defects in the synthesized compounds. It represents the width of the exponential tail in the absorption spectrum near the optical band edge, which arises from localized electronic states extending into the forbidden gap. Generally, lower "E_u" values reflect a more ordered lattice with fewer defects, whereas higher values suggest increased disorder and stronger carrier localization.[41,42] According to the Urbach rule, the degree of disorder can be extracted from the exponential relationship between the absorption coefficient (α) and the photon energy ($h\nu$), expressed as:[43]

$$\ln(\alpha) = \ln(\alpha_0) + \frac{h\nu}{E_u} \quad (3)$$

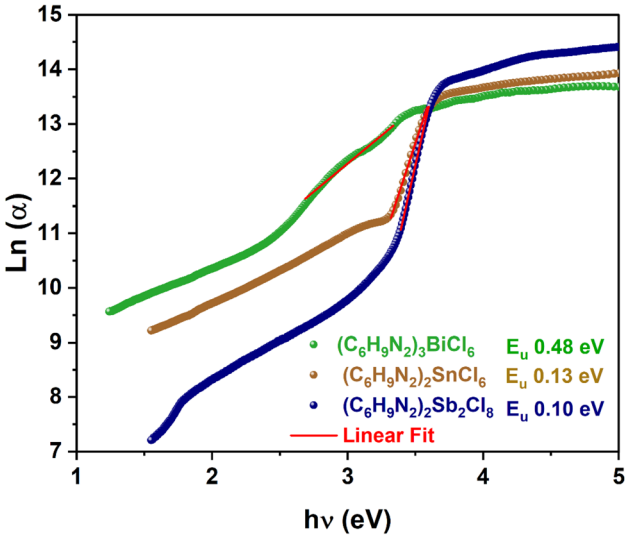

Fig. 7 Plot of ln(α)*versus* photon energy ($h\nu$) used for the determination of the Urbach energy (E_u).

Fig. 7 presents the plot of the natural logarithm of the absorption coefficient (ln(α)) *versus* photon energy ($h\nu$) for the investigated halometallate compounds. The Urbach energies derived from these plots are 0.10 eV for $(C_6H_9N_2)_2[Sb_2Cl_8]$, 0.13 eV for $(C_6H_9N_2)_2SnCl_6$, and 0.48 eV for $(C_6H_9N_2)_3[BiCl_6]$. The relatively low (E_u) values of the Sb- and Sn-based compounds indicate well-ordered lattices with minimal absorption tailing, reflecting fewer structural defects and higher crystalline regularity. In contrast, the Bi-containing material shows a substantially higher Urbach energy, pointing to greater structural disorder. This increased disorder is likely related to the larger ionic radius of Bi^{3+}, stronger spin–orbit interactions, and the pronounced effect of the stereochemically active ns^2 lone pair.[9,44] Such lattice irregularities in the Bi compound may also play a role in its reduced optical band gap, consistent with enhanced metal–halide orbital overlap and the presence of localized states near the band edges. It should be noted that a more direct confirmation of structural disorder would require complementary techniques such as TEM, Raman spectroscopy, or quantitative defect analysis.

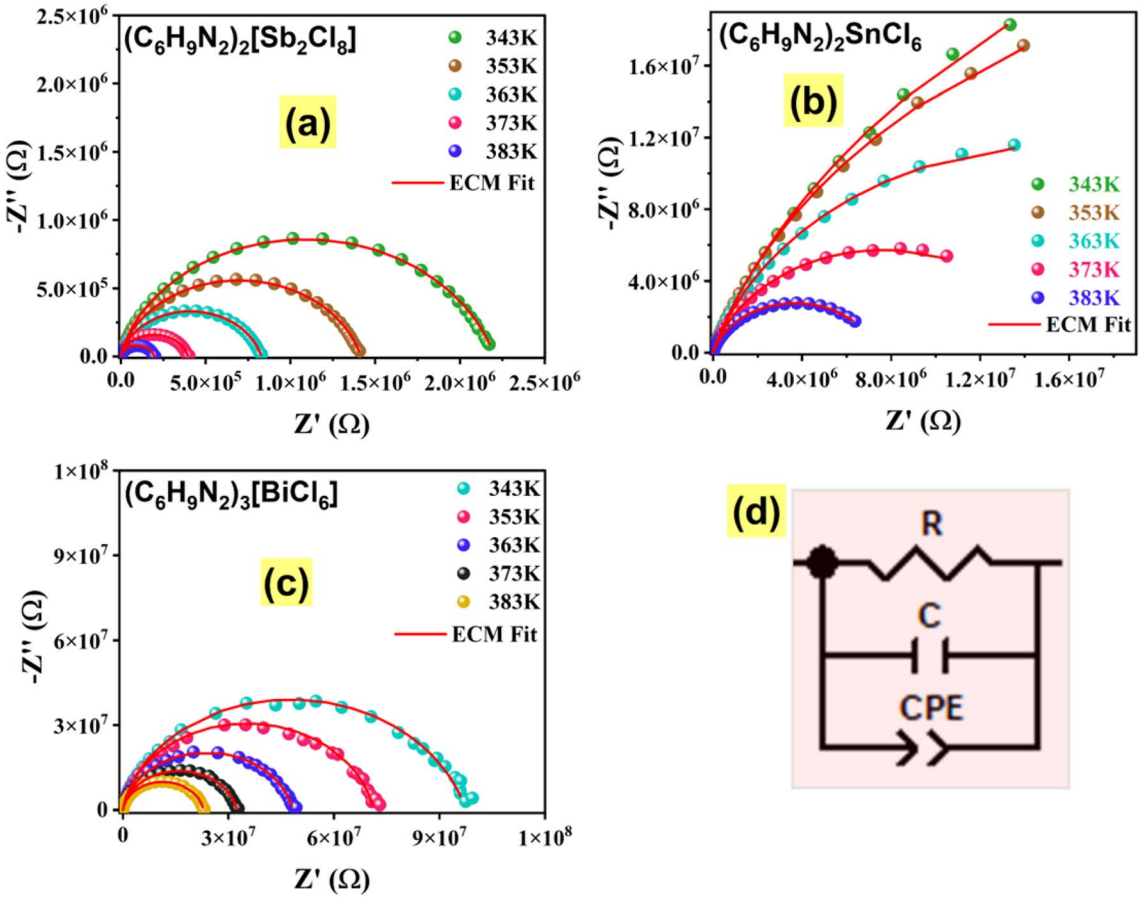

Fig. 8 Nyquist diagrams of 2-amino-5-methylpyridinium-based compounds, showing a decrease in bulk resistance with increasing temperature: (a) $(C_6H_9N_2)_2[Sb_2Cl_8]$, (b) $(C_6H_9N_2)_2SnCl_6$, (c) $(C_6H_9N_2)_3[BiCl_6]$ and (d) the corresponding equivalent circuit model.

3.4. Electrical properties investigated *via* complex impedance spectroscopy (CIS)

3.4.1. Impedance interpretation. Impedance spectroscopy (IS) is a reliable and extensively employed technique for exploring charge transport processes and negative temperature coefficient of resistance (NTCR) behavior in functional materials.[45] The electrical response of such materials is strongly dependent on their intrinsic structural characteristics.[46] In the present study, the complex impedance (Z^*) and electrical conductivity (σ) are treated as complementary formalisms that together provide a comprehensive description of the electrical properties and NTCR effect in the investigated 2-amino-5-methylpyridinium-based compounds. The complex impedance is composed of a real component (Z'), which corresponds to the resistive contribution, and an imaginary component (Z''), which reflects the reactive (capacitive) response of the material. It is mathematically expressed as:[47]

$$Z^* = Z' + jZ'' \quad (4)$$

The Nyquist plot (Z'' *versus* Z') is a fundamental graphical representation used to evaluate dielectric relaxation phenomena. For an ideal Debye relaxation process, this representation produces a perfect semicircle centered on the real axis, indicating a single, well-defined relaxation time. In contrast, practical materials typically display depressed or asymmetric semicircular arcs, revealing the presence of a distribution of relaxation times and non-ideal relaxation behavior.[47] In the present investigation, the Nyquist diagrams of the 2-amino-5-methylpyridinium-based compounds (M = Sb, Sn, Bi) recorded over the temperature range 343–383 K (Fig. 8(a–c)) exhibit well-defined semicircular features. The observed semicircles are depressed and slightly asymmetric, reflecting non-ideal relaxation behavior.[48] Their progressive shrinkage with rising temperature confirms the thermally activated nature of charge transport. Typically, the appearance of a single semicircular arc in a Nyquist representation is associated with the dominant contribution of the grain (bulk) response. As the temperature increases, the continuous reduction in arc diameter signifies a decrease in resistive behavior and an enhancement in conductivity, supporting the semiconducting character of $(C_6H_9N_2)_2[Sb_2Cl_8]$, $(C_6H_9N_2)_2SnCl_6$, and $(C_6H_9N_2)_3[BiCl_6]$, in agreement with the optical analysis discussed previously.[49]

The impedance spectra were quantitatively evaluated using the Z_{view} fitting program.[50] As shown in Fig. 8(a–c), an excellent correspondence is obtained between the experimental data and the simulated curves generated from the fitting procedure. The electrical response of the RE–HESZ ceramic can be satisfactorily

Table 4 Fitted electrical circuit parameters of 2-amino-5-methylpyridine-based samples measured at various temperatures (343–383 K)

T (K)	R (10^6 Ω)	C (10^{-11} F)	Q (10^{-10} F)	α	τ (s)
$(C_6H_9N_2)_3[BiCl_6]$					
383	22.5668	4.09167	1.01595	0.81739	5.90×10^{-4}
373	32.1464	2.76566	1.1657	0.86017	1.51×10^{-3}
363	44.8858	5.06084	1.03958	0.78132	1.04×10^{-3}
353	67.6201	6.89434	1.96215	0.55683	4.25×10^{-4}
343	96.2001	5.33588	1.81857	0.70886	3.32×10^{-3}
$(C_6H_9N_2)_2SnCl_6$					
383	7.44	1.834	5.202	0.78308	8.31×10^{-4}
373	15.523	2.022	4.801	0.77935	1.86×10^{-3}
363	31.5	2.406	5.200	0.75559	4.33×10^{-3}
353	58.2	2.413	4.950	0.75465	9.09×10^{-3}
343	78.0	2.585	5.650	0.73195	1.40×10^{-2}
$(C_6H_9N_2)_2[Sb_2Cl_8]$					
383	1.9582	1.840	3.522	0.81182	7.48×10^{-6}
373	3.9529	1.911	3.456	0.80881	1.67×10^{-5}
363	8.2884	2.033	3.417	0.80251	3.79×10^{-5}
353	14.159	2.082	3.575	0.79629	7.26×10^{-5}
343	22.053	2.170	3.839	0.78625	1.24×10^{-4}

described by an equivalent circuit model consisting of a grain resistance (R) connected in parallel with an ideal capacitor (C) and a constant phase element (CPE) (Fig. 8(d)). The CPE component is introduced to account for deviations from ideal capacitive behavior, which arise from structural heterogeneity, a distribution of relaxation times, and non-Debye-type relaxation effects. The impedance of the constant phase element is expressed by the following relation:[51]

$$Z_{CPE} = \frac{1}{Q(j\omega)^{\alpha}} \quad (5)$$

where "Q" is the CPE constant, "ω" is the angular frequency, and "α" ($0 \leq \alpha \leq 1$) describes the degree of deviation from ideal capacitive behavior.

The temperature dependence of the fitting parameters (R, C, Q, and α) is presented in Table 4. The impedance parameters (R, C, Q, α, and τ) provide a coherent picture of the relationship between structural characteristics and dielectric properties in the investigated compounds. In all cases, the resistance increases as temperature decreases, indicating that charge transport is thermally activated. The Bi-based compound exhibits the highest resistance, suggesting pronounced charge carrier localization, whereas the Sb-based compound shows the lowest resistance, consistent with enhanced carrier mobility. The capacitance values, of the order of 10^{-11} F, are typical of interfacial polarization processes and appear more stable in the Sn-based system, pointing to a more homogeneous dielectric response. Similarly, the CPE parameter (Q) is higher and more stable for the Sn compound, reflecting stronger and more uniform polarization compared with the more structurally disordered Bi and Sb systems. The α parameter highlights the degree of non-ideality in the relaxation process: the Bi compound exhibits the strongest deviation from Debye behavior due to significant structural distortion associated with the stereochemically active Bi^{3+} lone pair, whereas the Sn-based compound tends toward a more ideal relaxation response. The relaxation time, determined from $\tau = (RQ)^{(1/\alpha)}$,[16] indicates that the Sb-based compound exhibits the fastest dielectric relaxation, followed by the Bi system, while the Sn compound shows the slowest dynamics, consistent with a more ordered structure and thermally governed polarization mechanism. Overall, these results clearly demonstrate that the dielectric behavior is strongly influenced by the nature of the metal center, where lone-pair activity and structural distortion play a decisive role in controlling charge transport and relaxation processes.

Fig. 9(a–c) present the variation of electrical resistance (R) with temperature for $(C_6H_9N_2)_2[Sb_2Cl_8]$, $(C_6H_9N_2)_2SnCl_6$, and

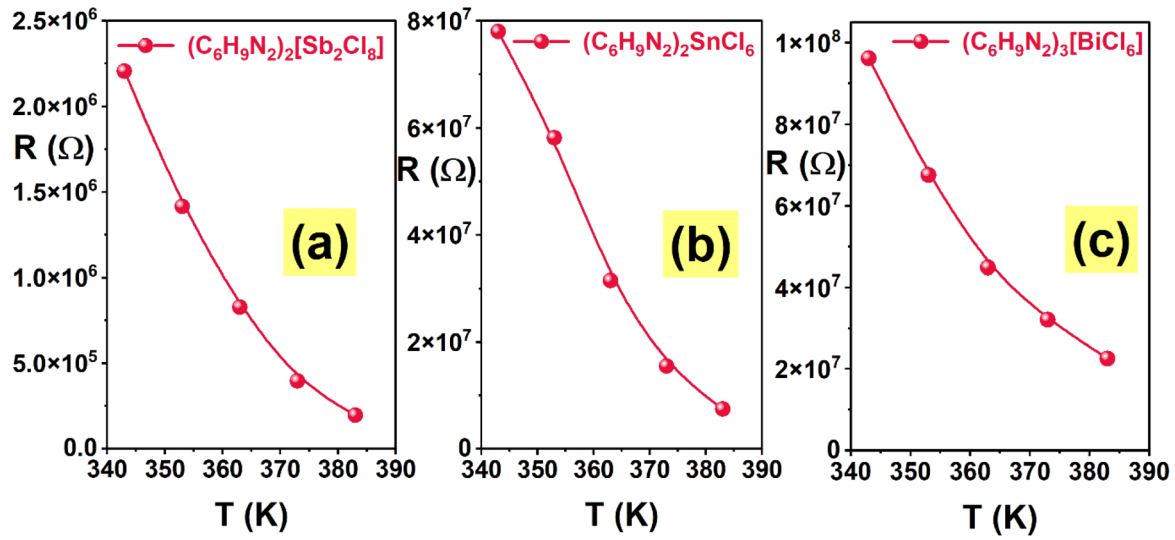

Fig. 9 Variation of electrical resistance as a function of temperature for 2-amino-5-methylpyridinium-based compounds, confirming the NTCR behavior: (a) $(C_6H_9N_2)_2[Sb_2Cl_8]$, (b) $(C_6H_9N_2)_2SnCl_6$, (c) $(C_6H_9N_2)_3[BiCl_6]$.

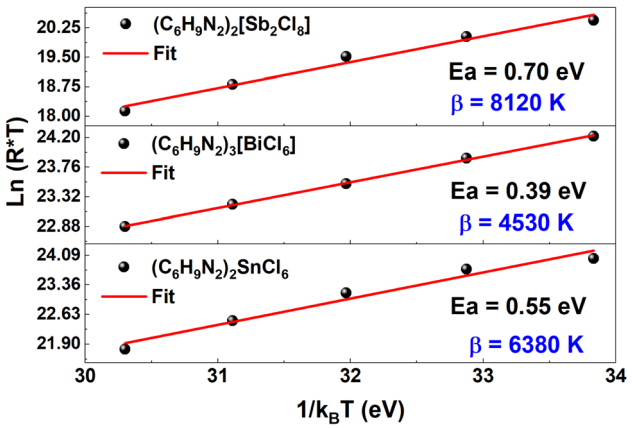

Fig. 10 Variation of ln(R*T) as a function of 1/$k_B T$.

$(C_6H_9N_2)_3[BiCl_6]$ over the temperature interval 343–383 K. For all investigated compounds, the resistance progressively decreases as the temperature increases. Such a trend is typical of materials exhibiting a negative temperature coefficient of resistance (NTCR).[52] In NTCR systems, thermal activation enhances the number and/or mobility of charge carriers, which facilitates their transport through the lattice and consequently lowers the resistive contribution.[53] The steady and progressive decrease in resistance with increasing temperature verifies the semiconducting character of the three compounds. In addition, the smooth $R(T)$ profiles, without anomalies or abrupt changes, indicate the absence of any structural phase transition within the investigated temperature interval. The strong sensitivity of resistance to temperature further supports a thermally activated conduction mechanism, likely dominated by carrier hopping between localized states. In summary, the temperature-dependent resistance behavior clearly evidences NTCR characteristics for $(C_6H_9N_2)_2[Sb_2Cl_8]$, $(C_6H_9N_2)_2SnCl_6$, and $(C_6H_9N_2)_3[BiCl_6]$, in agreement with their semiconducting nature.

The evaluation of the activation energy is an essential parameter for understanding the electrical transport mechanism. Fig. 10 presents the variation of ln(R*T) as a function of 1/($k_B T$). The activation energies were determined using the following relation:[54]

$$R = \frac{R_0}{T}\exp\left(\frac{-E_a}{k_B T}\right) \quad (6)$$

where R_0 is the pre-exponential factor, E_a is the activation energy, and k_B is the Boltzmann constant. From the linear fitting of the experimental data, the activation energies were found to be 0.70 eV for $(C_6H_9N_2)_2[Sb_2Cl_8]$, 0.55 eV for $(C_6H_9N_2)_2SnCl_6$, and 0.39 eV for $(C_6H_9N_2)_3[BiCl_6]$. The NTC thermistor constant β, which is directly related to the activation energy, can be expressed as:[55]

$$\beta = \frac{E_a}{k_B} \quad (7)$$

where E_a is the activation energy and k_B is the Boltzmann constant. The calculated "β" values are approximately 8240 K for $(C_6H_9N_2)_2[Sb_2Cl_8]$, 6270 K for $(C_6H_9N_2)_2SnCl_6$, and 4640 K for $(C_6H_9N_2)_3[BiCl_6]$, which are comparable to those reported for other NTC materials.[56,57]

3.4.2. Electrical conductivity and activation energy analysis. An alternative approach based on electrical conductivity analysis offers valuable insight into the frequency-dependent mobility of charge carriers, thereby improving the understanding of transport mechanisms within the material. This method also provides information about the distribution of the electric field and its influence on charge dynamics under an applied excitation.

The real part of the electrical conductivity was calculated from the impedance components (Z' and Z'') using the following expression:[58]

$$\sigma = \frac{e}{d}\frac{Z'}{\left(Z'^2 + Z''^2\right)} \quad (8)$$

where "e" corresponds to the sample thickness and "d" represents the cross-sectional area of the pellet.

Fig. 11(a–c) illustrates the frequency dependence of the total electrical conductivity measured between 343 and 383 K. For all three compounds, the conductivity systematically rises as the temperature increases, indicating that charge transport is governed by a thermally activated mechanism in $(C_6H_9N_2)_2[Sb_2Cl_8]$, $(C_6H_9N_2)_2SnCl_6$, and $(C_6H_9N_2)_3[BiCl_6]$. The conductivity spectra exhibit two distinct regions. In the low-frequency domain, a nearly frequency-independent plateau is observed, corresponding to the direct current conductivity (σ_{dc}). In this regime, σ_{dc} increases with temperature, reflecting enhanced carrier mobility and/or carrier concentration.[47] At higher frequencies, the conductivity displays a dispersive behavior characteristic of alternating current conductivity (σ_{ac}). In this region, σ becomes strongly frequency dependent and progressively increases with frequency. This dispersion is commonly associated with localized hopping of charge carriers between neighboring sites. The growth of σ_{ac} with temperature suggests that additional hopping pathways become accessible and that a larger number of charge carriers participate in the transport process.

Such frequency-dependent conductivity behavior follows Jonscher's universal power law, which successfully describes the ac conduction mechanism in disordered and semiconducting materials:[59]

$$\sigma(\omega, T) = \sigma_{dc}(T) + \sigma_{ac}(\omega, T) \quad (9)$$

$$\sigma(\omega, T) = \sigma_{dc}(T) + A\omega^{S(T)} \quad (10)$$

In this framework, σ_{dc} denotes the frequency-independent conductivity observed in the low-frequency region, whereas σ_{ac} describes the conductivity contribution dominant at higher frequencies. The parameter "A" is a constant that varies with temperature, while the exponent "s" in the power law characterizes the interaction strength between charge carriers and their local structural surroundings.

Fig. 11(d) presents the frequency-dependent conductivity of the investigated compounds at 343 K. The observed conductivity decreases in the sequence $(C_6H_9N_2)_2[Sb_2Cl_8]$ >

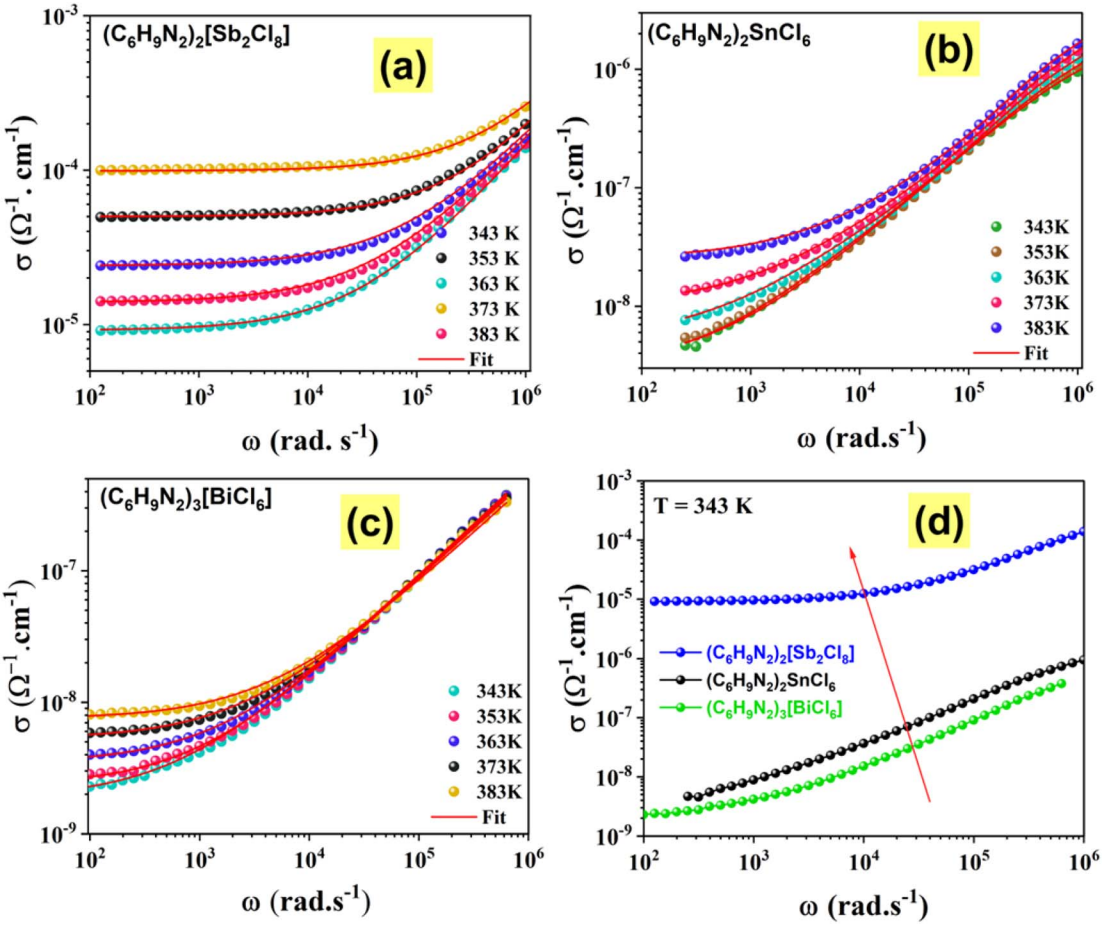

Fig. 11 Temperature dependence of electrical conductivity for 2-amino-5-methylpyridinium-based compounds: (a) $(C_6H_9N_2)_2[Sb_2Cl_8]$, (b) $(C_6H_9N_2)_2SnCl_6$, (c) $(C_6H_9N_2)_3[BiCl_6]$, and (d) comparison of electrical conductivity at 343 K.

$(C_6H_9N_2)_2SnCl_6$ > $(C_6H_9N_2)_2[BiCl_6]$, revealing clear differences in charge transport efficiency. The Sb-based material exhibits the highest conductivity, indicating that its crystal structure and bonding network facilitate easier movement of charge carriers, supporting both long-range dc transport and short-range hopping processes. Conversely, the Bi-based compound shows the lowest conductivity, likely due to enhanced lattice distortion, stronger spin–orbit interactions, and the effect of the stereochemically active Bi^{3+} lone pair, which together reduce carrier mobility. The Sn-based compound displays intermediate behavior, consistent with its structural and electronic features. These trends emphasize the critical influence of the metal cation on charge transport, highlighting how structural and electronic factors govern the interplay between delocalized conduction and localized hopping in these hybrid halometallates.

To obtain deeper understanding of the charge-transport behavior, the temperature dependence of the direct current conductivity (σ_{dc}) of the prepared materials was thoroughly examined. The analysis was carried out using the Arrhenius formalism, commonly applied to describe thermally activated conduction mechanisms:[60]

$$\sigma_{dc} = \frac{\sigma_0}{T} e^{\left(\frac{-E_a}{k_B T}\right)} \quad (11)$$

In this relation, σ_0 denotes the pre-exponential constant, E_a corresponds to the activation energy, and k_B is the Boltzmann constant. The nature of the conduction process was clarified by examining the temperature dependence of the electrical conductivity through the representation of $\ln(\sigma_{dc}*T)$ as a function of 1000/T (Fig. 12(a–c)). The observed straight-line variation demonstrates that the electrical conduction is governed by a thermally activated process consistent with the Arrhenius model. The fact that this linear trend is maintained for all investigated compositions reveals that substituting the central metal ion (Sb, Sn, or Bi) does not alter the underlying transport mechanism, but instead affects the conductivity level and the corresponding activation barrier. The calculated activation energies 0.71 eV for $(C_6H_9N_2)_2[Sb_2Cl_8]$, 0.54 eV for $(C_6H_9N_2)_2SnCl_6$, and 0.40 eV for $(C_6H_9N_2)_3[BiCl_6]$ are characteristic of a small polaron hopping process.[61,62] In this mechanism, charge carriers are localized and migrate between adjacent sites *via* thermally assisted hopping, strongly influenced by electron–lattice interactions. The progressive decrease in activation energy from (Sb) to (Bi) indicates that carrier transport becomes

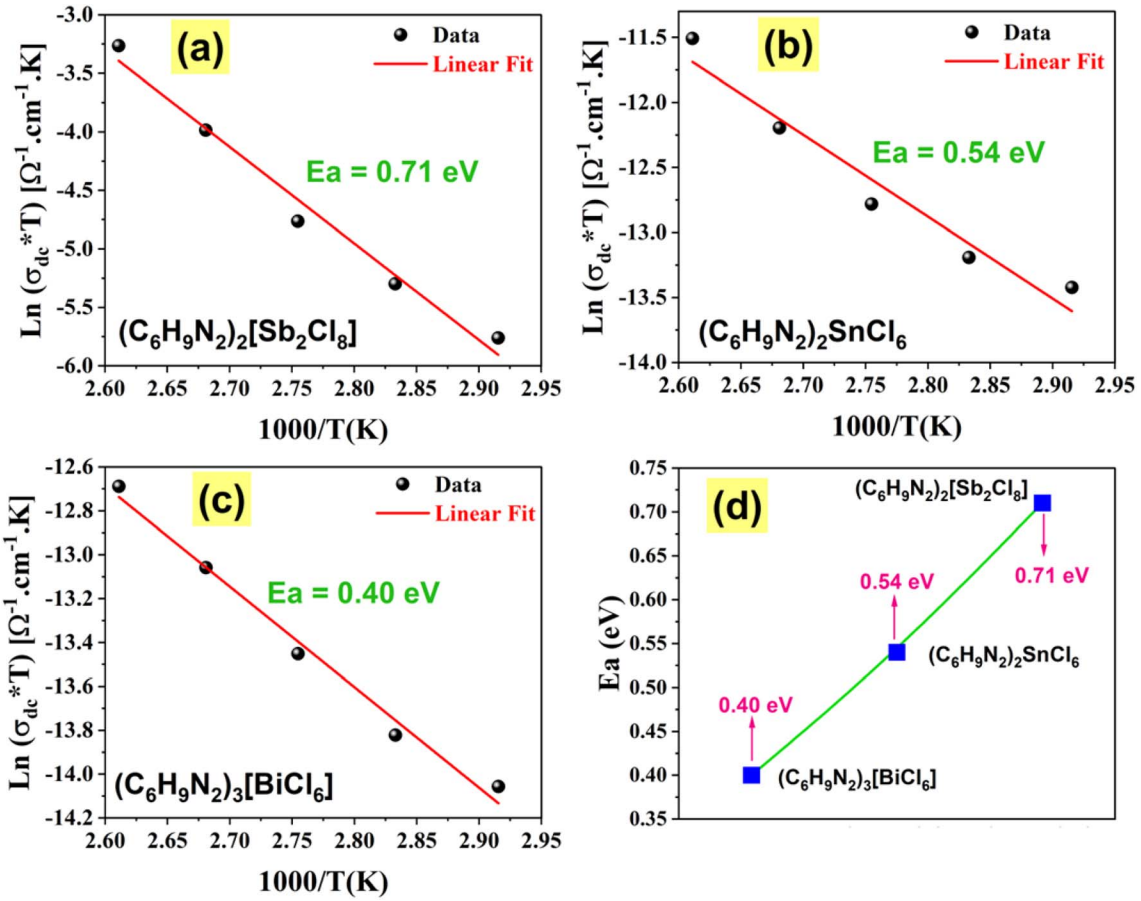

Fig. 12 Variation of dc conductivity, ln(σ_{dc}*T), as a function of (1000/T) for 2-amino-5-methylpyridinium-based compounds: (a) $(C_6H_9N_2)_2[Sb_2Cl_8]$, (b) $(C_6H_9N_2)_2SnCl_6$, (c) $(C_6H_9N_2)_3[BiCl_6]$ and (d) variation of the activation energy, showing a progressive increase in activation energy from Bi- to Sb-based compounds.

increasingly favorable with heavier metal cations (Fig. 12(d)), likely as a result of greater structural polarizability and enhanced orbital overlap, which together promote improved charge mobility in the Bi-based material.

The lower conductivity observed in the Bi-based compound, despite its relatively lower activation energy, can be explained by microstructural and defect-related effects. The presence of the stereochemically active Bi^{3+} lone pair induces local structural distortions, which enhance defect density and increase grain boundary resistance. These features promote charge carrier localization and scattering, limiting long-range transport. In this context, electrical conduction is governed not only by thermally activated hopping but also by grain boundary barriers and possible polaronic effects, which together reduce the overall conductivity of the Bi-based system.

A comparative analysis emphasizes the crucial role of structural disorder in controlling charge transport in the Sb-, Sn-, and Bi-based compounds. The Bi-based system exhibits the highest degree of disorder, primarily due to the stereochemically active Bi^{3+} lone pair, which induces significant local lattice distortions and increases defect density. These effects promote charge carrier localization and scattering, thereby limiting electrical conductivity. In contrast, the Sb-based compound displays the lowest degree of disorder and the highest conductivity, indicating more efficient charge transport. The Sn-based system shows intermediate behavior, consistent with its moderately ordered structure characterized by relatively regular octahedral units. Overall, this comparison demonstrates that structural disorder strongly influences the electrical properties, with increased disorder leading to reduced carrier mobility and modified relaxation dynamics.

Table 5 compiles the activation energy (E_a) values related to charge transport in Sn-, Sb-, and Bi-based organic–inorganic hybrid compounds.

Table 5 Activation energy values (E_a) reported for (Sn, Sb, Bi)-based organic–inorganic hybrid materials

Compounds	Activation energy: E_a (eV)	References
$(C_6H_9N_2)_2[Sb_2Cl_8]$	0.71	This work
$(C_6H_9N_2)_2SnCl_6$	0.54	This work
$(C_6H_9N_2)_3[BiCl_6]$	0.40	This work
$(CH_3NH_3)_2SnBr_6$	0.61	32
$[(C_2H_5)_4N]_3Bi_2I_9$	0.55	63
$(C_6H_9N_2)_2SnBr_6$	0.85	3
$(C_6H_9N_2)_3[BiBr_6]H_2O$	0.51–0.91	44
$[C_5H_6N_2Cl]_2[Sb_2Cl_8]$	0.85	64

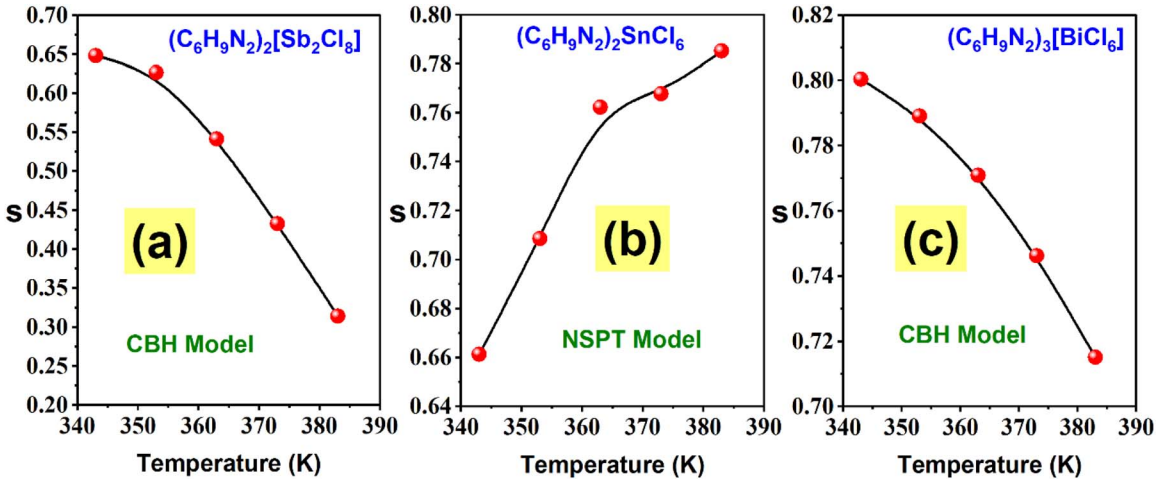

Fig. 13 Temperature dependence of the frequency exponent "*s*" for 2-amino-5-methylpyridinium-based compounds: (a) $(C_6H_9N_2)_2[Sb_2Cl_8]$, (b) $(C_6H_9N_2)_2SnCl_6$, (c) $(C_6H_9N_2)_3[BiCl_6]$.

A comparison with previously reported data shows that these values are consistent with those found in similar hybrid halide systems. For instance, $(CH_3NH_3)_2SnBr_6$ (0.61 eV)[32] and $[(C_2H_5)_4N]_3Bi_2I_9$ (0.55 eV)[63] present close activation energies, indicating analogous transport behavior. In contrast, larger values such as 0.85 eV, reported for $(C_6H_9N_2)_2SnBr_6$ (ref. 3) and $[C_5H_6N_2Cl]_2[Sb_2Cl_8]$[64], reflect stronger carrier localization and higher barriers to hopping conduction. Conversely, the lower E_a measured for the Bi-based compound points to improved carrier mobility. The differences in activation energy arise from several contributing factors. The nature of the metal ion plays a central role, as the electronic structures of Sb^{3+}, Sn^{4+}, and Bi^{3+} govern the band structure and transport pathways. The type of halide (Cl^-, Br^-, I^-) also influences lattice polarizability and bonding character, thereby affecting the energy required for carrier motion. In addition, structural aspects such as octahedral distortion and the connectivity of inorganic units significantly impact charge transport. Concerning the conductivity, its variation with temperature exhibits a typical thermally activated trend, consistent with what has been reported for similar hybrid halide materials.[3,32,63,64] Taken together, the activation energy and conductivity findings align well with literature data, indicating that charge transport in these compounds is dominated by a thermally activated hopping mechanism. The observed differences can be attributed to variations in the metal cation, the nature of the halide, and the structural features of the materials.

To clarify the prevailing AC transport mechanism, the temperature-dependent behavior of the frequency exponent "*s*" was analyzed for the 2-amino-5-methylpyridinium-based materials (Fig. 13(a–c)). The manner in which "*s*" evolves with temperature serves as a key indicator of the underlying charge-transfer process in an alternating electric field. Various theoretical approaches have been developed to account for this dependence, notably the Quantum Mechanical Tunneling (QMT),[65] Correlated Barrier Hopping (CBH),[66] Non-Overlapping Small Polaron Tunneling (NSPT),[67] and Overlapping Large Polaron Tunneling (OLPT)[68] models.

The experimental trend of "*s*" as a function of temperature reveals that the AC conductivity of $(C_6H_9N_2)_2[Sb_2Cl_8]$ and $(C_6H_9N_2)_3[BiCl_6]$ is predominantly governed by the Correlated Barrier Hopping (CBH) mechanism, where charge carriers move between localized sites by surmounting Coulomb-correlated potential barriers. Conversely, the response of $(C_6H_9N_2)_2SnCl_6$ aligns more closely with the Non-Overlapping Small Polaron Tunneling (NSPT) model, pointing to a tunneling process involving localized polarons with negligible overlap of their wavefunctions.

4. Conclusion

This work presents a detailed examination of the structural, optical, and electrical characteristics of the hybrid materials $(C_6H_9N_2)_2[Sb_2Cl_8]$, $(C_6H_9N_2)_2SnCl_6$, and $(C_6H_9N_2)_3[BiCl_6]$, with the aim of clarifying how substitution of the metal center (Sb, Sn, Bi) influences their physical properties. Optical measurements indicate a progressive reduction in the band gap energy from Sb to Bi. The determined band gap values are 3.49 eV for $(C_6H_9N_2)_2[Sb_2Cl_8]$, 3.36 eV for $(C_6H_9N_2)_2SnCl_6$, and 3.10 eV for $(C_6H_9N_2)_3[BiCl_6]$. This gradual decrease can be associated with the higher atomic mass and stronger spin–orbit interaction of the heavier metal ions, which alter the electronic band structure and decrease the separation between valence and conduction bands. Electrical investigations reveal that DC conductivity follows a thermally activated Arrhenius-type mechanism. The activation energies were found to be 0.71 eV for the Sb-based compound, 0.54 eV for the Sn-based compound, and 0.40 eV for the Bi-based compound. The downward trend in activation energy from Sb to Bi suggests a continuous reduction in the energy barrier for charge carrier migration, leading to improved electrical transport. Despite the lower activation energy of the Bi-based compound, the overall conductivity decreases along the series: $(C_6H_9N_2)_2[Sb_2Cl_8]$ > $(C_6H_9N_2)_2SnCl_6$ > $(C_6H_9N_2)_3[BiCl_6]$. This trend indicates that other structural factors, such as lattice connectivity, carrier concentration, and orbital overlap, play a dominant role in controlling the charge transport,

overriding the effect of activation energy alone. The Sb-containing compound, with the highest conductivity, demonstrates that the choice of metal cation strongly impacts carrier mobility, highlighting the potential of these materials for applications requiring efficient charge transport.

Overall, metal substitution represents an effective and versatile approach for tuning the electronic structure and charge transport properties of 2-amino-5-methylpyridinium-based hybrid materials, highlighting their potential for semiconducting and electronic applications. Future work will focus on the fabrication and optimization of thin films to enable device integration. In addition, photoconductivity measurements and device-level studies will be conducted to further elucidate and validate their optoelectronic performance.

Author contributions

Mohamed Loucif: investigation, data curation, formal analysis, visualization, writing—original draft, writing—review and editing. Iheb Garoui: investigation, data curation, formal analysis, visualization, writing—original draft, writing—review and editing. Souad Chkoundali: supervision, resources, validation, methodology, review and editing. Rima Mohammed Altalib: investigation, data curation, formal analysis, visualization, writing—original draft, writing—review and editing. Mehdi Akermi: investigation, formal analysis, visualization, writing—original draft, writing. Abderrazek Oueslati: conceptualization, methodology, formal analysis, validation, writing review and editing.

Conflicts of interest

The authors declare that they have no known competing financial interests or personal relationships that could have appeared to influence the work reported in this paper. All persons who have participated in this work are listed as authors.

Data availability

The authors confirm that the data used to support the findings of this study are included within the article and are available from the corresponding author upon reasonable request.

Acknowledgements

The authors gratefully acknowledge the funding of the Deanship of Graduate Studies and Scientific Research, Jazan University, Saudi Arabia, through Project Number: (JU-20260253-DGSSR-ORA-2026).

References

1 K. Zhou, B. Qi, Z. Liu, X. Wang, Y. Sun and L. Zhang, Advanced Organic–Inorganic Hybrid Materials for Optoelectronic Applications, *Adv. Funct. Mater.*, 2024, **34**(52), 2411671, DOI: 10.1002/adfm.202411671.

2 S. Dgachi, A. M. Ben Salah, M. M. Turnbull, T. Bataille and H. Naïli, Investigations on (C6H9N2)2[MIIBr4] halogenometallate complexes with MII = Co, Cu and Zn: Crystal structure, thermal behavior and magnetic properties, *J. Alloys Compd.*, 2017, **726**, 315–322, DOI: 10.1016/j.jallcom.2017.07.278.

3 I. Garoui, N. Weslati, I. Chaabane, N. A. Alghamdi, M. Tliha and A. Oueslati, Impact of halogen substitution on the structural, optical, and dielectric behavior of (C6H9N2)2SnX6 (X = Cl, Br) for optoelectronic device integration, *Opt. Mater.*, 2026, **169**, 117651, DOI: 10.1016/j.optmat.2025.117651.

4 L. Saidi, A. Samet, T. Dammak, S. Pillet and Y. Abid, Down and up conversion luminescence of the lead-free organic metal halide material: (C9H8NO)2SnCl6·2H2O, *Phys. Chem. Chem. Phys.*, 2021, **23**(29), 15574–15581, DOI: 10.1039/d1cp01702k.

5 A. Alibi, N. Elleuch, A. Oueslati, S. Shova and M. Boujelbene, Synthesis, optical features, and electrical properties of a new antimony-based hybrid halide (C8H14N2)[SbCl5], *RSC Adv.*, 2025, **15**(54), 45840–45854, DOI: 10.1039/d5ra06615h.

6 A. S. Rao, U. Baruah and S. K. Das, Stabilization of [BiCl6]3− and [Bi2Cl10]4− with various organic precursors as cations leading to inorganic–organic supramolecular adducts: Syntheses, crystal structures and properties of [C5H7N2]3[BiCl6], [C5H7N2][C5H8N2][BiCl6] and [C10H10N2]2[Bi2Cl10], *Inorg. Chim. Acta*, 2011, **372**(1), 206–212, DOI: 10.1016/j.ica.2011.01.109.

7 K. B. Brahim, H. Nejeh, N. Weslati, M. Tliha, S. Znaidia and A. Oueslati, Structural and optical properties of semiconductor organic–inorganic hybrid components ([N(CnH2n+1)4]2SnBr6 (n = 1;2)): Potential applications in solar cells, LEDs and photodetectors, *Inorg. Chem. Commun.*, 2025, **171**, 113555, DOI: 10.1016/j.inoche.2024.113555.

8 A. Elghoul, *et al.*, Investigation on the structural, optical, photoluminescence and electric properties of a semiconductor material [Br(CH2)2N(CH3)3]2SnBr6, *RSC Adv.*, 2025, **15**(47), 40199–40208, DOI: 10.1039/d5ra06415e.

9 R. Altalib, *et al.*, A zero-dimensional (C6H9N2)3[BiCl6] hybrid material: synthesis and structural, optical, and electrical conductivity, *RSC Adv.*, 2025, **15**(41), 33946–33961, DOI: 10.1039/d5ra01766a.

10 A. Alibi, *et al.*, Comprehensive structure–property–function correlation in three hybrid Bi(<scp>iii</scp>) and Sb(<scp>iii</scp>) metal halide compounds based on 4-ethylaminomethylpyridine: comparative insights into optical, dielectric, and antibiological activities, *Mater. Adv.*, 2026, **7**(3), 1737–1756, DOI: 10.1039/d5ma01261a.

11 Y. Chen, *et al.*, Bidirectional Photoregulated Chromism in Pyridinium Derivatives *via* Secondary Excitation-Driven Electron Transfer, *Angew. Chem.*, 2025, **138**(6), 23781, DOI: 10.1002/ange.202523781.

12 H. Tlili, *et al.*, Synthesis, crystal structure, and multifunctional properties of a tetrabromomercurate(II) hybrid with protonated 4-(dimethylamino)pyridine,

Polyhedron, 2026, **285**, 117929, DOI: 10.1016/j.poly.2025.117929.

13 W. Hallab, *et al.*, A new multifunctional copper iodide–pyrazine hybrid for sensitive creatinine detection in biological samples: synthesis, structural features, characterization, and electrochemical evaluation, *J. Mater. Chem. B*, 2025, **13**(40), 13088–13097, DOI: 10.1039/d5tb01035g.

14 U. Sizir, D. A. Kose and O. Yurdakul, Synthesis, spectroscopic and thermal characterization of non-metal cation (nmc) pentaborates salts containing 2-amino-5-nitropyridine and 2-amino-6-methylpyridine as cation, *Hittite j. sci. eng.*, 2015, **2**(1), 91–96, DOI: 10.17350/hjse19030000014.

15 X. Wei, *et al.*, Synthesis, structure, and photoelectric properties of a novel zero-dimensional organic-inorganic hybrid perovskite (C6H9N2)2MnI4, *Opt. Mater.*, 2023, **136**, 113360, DOI: 10.1016/j.optmat.2022.113360.

16 A. Ghoudi, *et al.*, Optical and electric properties of the organic-inorganic hybrid bis(2-amino-5-picolinium) Tetrachlorocobaltate(II) [(C6H9N2)2CoCl4], *Inorg. Chem. Commun.*, 2024, **168**, 112925, DOI: 10.1016/j.inoche.2024.112925.

17 J. He, *et al.*, Synthesis, Structure, and Photoelectric Properties of a Novel 0-Dimensional Organic–Inorganic Hybrid Perovskite (2-5-py)2MnBr4, *J. Phys. Chem. C*, 2021, **125**(41), 22898–22906, DOI: 10.1021/acs.jpcc.1c07221.

18 I. Jomaa, *et al.*, Synthesis of 2-amino-5-methylpyridinium tetrachloridocadmate(II) (C6H9N2)2[CdCl4]: Structure, DFT-calculated descriptors and molecular docking study, *J. King Saud Univ., Sci.*, 2024, **36**(5), 103178, DOI: 10.1016/j.jksus.2024.103178.

19 A. Ghoudi, *et al.*, Crystal structure and optical characterization of a new hybrid compound, C6H9N2FeCl4, with large dielectric constants for field-effect transistors, *RSC Adv.*, 2023, **13**(19), 12844–12862, DOI: 10.1039/d3ra01239e.

20 I. Chaabane, W. Rekik, M. Zaghrioui, J. Lhoste, A. Oueslati and M. Gargouri, Synthesis, crystal structure, and ionic conductivity of a new organic–inorganic bromides (C6H9N2)2[SbBr4]Br, *Ionics*, 2024, **30**(9), 5827–5844, DOI: 10.1007/s11581-024-05680-5.

21 I. Chaabane, W. Rekik, H. Ghalla, M. Zaghrioui, J. Lhoste and A. Oueslati, Crystal structure, optical characterization, conduction and relaxation mechanisms of a new hybrid compound (C6H9N2)2[Sb2Cl8], *RSC Adv.*, 2024, **14**(5), 3588–3598, DOI: 10.1039/d3ra08885e.

22 I. Garoui, *et al.*, Synthesis, crystal structure, BFDH morphology, Hirshfeld surface analysis and electrical characterization of the new bi-(2-amino-5-methylpyridinium) hexa-chlorostannate compound, *Phys. E*, 2024, **158**, 115897, DOI: 10.1016/j.physe.2024.115897.

23 A. S. Albrecht, C. P. Landee and M. M. Turnbull, Structure of bis(2-amino-5-methylpyridinium) tetrachlorozincate at 298 and 150 K, *J. Chem. Crystallogr.*, 2003, **33**(4), 269–276, DOI: 10.1023/a:1023829127254.

24 A. Singh, S. K. Gupta and C. M. S. Negi, Lead-free Formamidinium Bismuth Bromide Perovskites for Memristor applications: a lead-free approach to sustainable electronics, *Emergent Mater.*, 2026, **9**(1–3), 5, DOI: 10.1007/s42247-026-01373-z.

25 V. Singh, N. Grover, P. B. Agarwal and P. Arora, Multiphysics Modeling and Optimization of High-Efficiency Lead-Free CH3NH3SnBr3 Perovskite Solar Cells, *Adv. Theory Simul.*, 2026, **9**(4), 70399, DOI: 10.1002/adts.70399.

26 S. Hermi, A. A. Alotaibi, F. Lefebvre, C. Ben Nasr and M. H. Mrad, Elaboration, crystal structure, physico-chemical characterization and theoretical investigation of a new non-centrosymmetric Sn(IV) complex (C4H12N2)[SnCl6]·3H2O, *J. Mol. Struct.*, 2020, **1216**, 128296, DOI: 10.1016/j.molstruc.2020.128296.

27 A. Rayes, C. B. Nasr and M. Rzaigui, Synthesis and structural characterization of a new layered chlorozincophosphate, Zn(HPO4)Cl·[H3N(CH2)6NH3]0.5, *Mater. Res. Bull.*, 2004, **39**(4–5), 571–580, DOI: 10.1016/j.materresbull.2003.12.016.

28 I. Garoui, *et al.*, Electronic Behavior, Charge-Carrier Transport Properties, and Dielectric Polarization of Lead-Free Sodium Metagermanate (Na2GeO3) Perovskite: Insights into Its Optoelectronic Potential, *J. Electron. Mater.*, 2026, **1**, 12813, DOI: 10.1007/s11664-026-12813-1.

29 Y. Chen, *et al.*, Effect of the Host Lattice Environment on the Expression of $5s^2$ Lone-Pair Electrons in a 0D Bismuth-Based Metal Halide, *Inorg. Chem.*, 2023, **62**(6), 2806–2816, DOI: 10.1021/acs.inorgchem.2c03961.

30 H. Arfin, *et al.*, ns^2 Electron (Bi^{3+} and Sb^{3+}) Doping in Lead-Free Metal Halide Perovskite Derivatives, *Chem. Mater.*, 2020, **32**(24), 10255–10267, DOI: 10.1021/acs.chemmater.0c03394.

31 D. Louër, T. Bataille, T. Roisnel and J. Rodriguez-Carvajal, A study of nanocrystalline yttrium oxide from diffraction-line-profile analysis: comparison of methods and crystallite growth, *Powder Diffr.*, 2002, **17**(4), 262–269, DOI: 10.1154/1.1523077.

32 I. Ibrahmi, *et al.*, Synthesis and trigonal structure of a new lead-free zero-dimensional perovskite (CH3NH3)2[SnBr6] with multifunctional optical and electrical properties, *J. Phys. Chem. Solids*, 2025, **207**, 112909, DOI: 10.1016/j.jpcs.2025.112909.

33 A. B. J. Kharrat, K. Kahouli and S. Chaabouni, Detailed investigation of the optical properties of the (C8H11BrN)3BiCl6 compound by UV–visible measurements, *Bull. Mater. Sci.*, 2020, **43**(1), 275, DOI: 10.1007/s12034-020-02248-7.

34 M. ben gzaiel, I. Garoui, F. N. Almutairi, I. Mbarek and A. Oueslati, Lead-Free halide perovskites for optoelectronic application: Investigation of structural, optical, electric and dielectric behaviors, *Opt. Mater.*, 2024, **154**, 115664, DOI: 10.1016/j.optmat.2024.115664.

35 R. D. Shannon, Revised effective ionic radii and systematic studies of interatomic distances in halides and chalcogenides, *Acta Crystallogr., Sect. A*, 1976, **32**(5), 751–767, DOI: 10.1107/s0567739476001551.

36 S. Jarboui, C. Hrizi, A. Oueslati and F. Zouari, Study on structural, optical, thermal and electrical properties of a new centrosymmetric compound (Qx-H)4Bi2Cl10, *Inorg.*

Chim. Acta, 2024, **561**, 121876, DOI: 10.1016/j.ica.2023.121876.

37 K. Kahouli, A. Ben Jazia Kharrat, M. S. M. Abdelbaky, S. García-Granda, K. Khirouni and S. Chaabouni, Synthesis, crystal structure, vibrational properties, optical properties and Hirshfeld surface analysis of a new Bi (III) halide complex: (C2H8N)3BiBr6 for optoelectronic devices, *Indian J. Phys.*, 2022, **97**(2), 457–472, DOI: 10.1007/s12648-022-02407-y.

38 K. Kahouli, A. B. J. Kharrat and S. Chaabouni, Optical properties analysis of the new (C9H14N)3BiCl6 compound by UV–visible measurements, *Indian J. Phys.*, 2021, **95**(12), 2797–2805, DOI: 10.1007/s12648-020-01942-w.

39 I. Tlili, R. Essalhi, G. Mousdi, M. S. M. Abdelbaky and S. Chaabouni, Synthesis and characterization of a new organic-inorganic hybrid material based on antimony, *J. Mol. Struct.*, 2022, **1251**, 132012, DOI: 10.1016/j.molstruc.2021.132012.

40 M. Mathlouthi, A. Valkonen, M. Rzaigui and W. Smirani, Structural characterization, spectroscopic, thermal, AC conductivity and dielectric properties and antimicrobial studies of (C8H12N)2[SnCl6], *Phase Transitions*, 2016, **90**(4), 399–414, DOI: 10.1080/01411594.2016.1212194.

41 G. D. Cody, T. Tiedje, B. Abeles, B. Brooks and Y. Goldstein, Disorder and the Optical-Absorption Edge of Hydrogenated Amorphous Silicon, *Phys. Rev. Lett.*, 1981, **47**(20), 1480–1483, DOI: 10.1103/physrevlett.47.1480.

42 M. Krimi, F. Hajlaoui, M. S. M. Abdelbaky, S. Garcia-Granda and A. Ben Rhaiem, Investigation of optical, dielectric, and conduction mechanism in lead-free perovskite CsMnBr3, *RSC Adv.*, 2024, **14**(15), 10219–10228, DOI: 10.1039/d4ra01151a.

43 F. Urbach, The Long-Wavelength Edge of Photographic Sensitivity and of the Electronic Absorption of Solids, *Phys. Rev.*, 1953, **92**(5), 1324, DOI: 10.1103/physrev.92.1324.

44 R. Altalib, *et al.*, Structure–property relationships in tris(2-amino-5-methylpyridinium) hexabromobismuthate monohydrate with a focus on optical and electrical behavior for optoelectronics applications, *RSC Adv.*, 2025, **15**(39), 32906–32918, DOI: 10.1039/d5ra04097c.

45 S. Panda and S. K. Parida, Studies on the structural, microstructure, dielectric, electrical and optical properties of Gd-doped BiFeO3 ceramic and its NTC thermistor application, *Mater. Adv.*, 2026, **10**, 3166, DOI: 10.1039/d5ma00885a.

46 I. Garoui, S. Ben Yahya, N. A. Alghamdi, I. Chaabane, A. Oueslati and B. Louati, Investigation of electronic parameters, carrier transport mechanisms *via* the correlated barrier hopping model, electrothermal NTCR effects, and polarization contributions to the dielectric response of Ni3(PO4)2 orthophosphates synthesized by the sintering process, *Mater. Adv.*, 2025, **6**(24), 9761–9778, DOI: 10.1039/d5ma01096a.

47 I. Garoui, *et al.*, New organic–inorganic chloride (2-amino-4-methylpyridinium hexachlorostannate): Crystal structure, BFDH morphology, and electrical conduction mechanism, *J. Phys. Chem. Solids*, 2025, **206**, 112840, DOI: 10.1016/j.jpcs.2025.112840.

48 A. Djemli, *et al.*, Synthesis, optical and electrical properties of (Ce0.2Nd0.2Sm0.2Ho0.2Yb0.2)2Zr2O7 high-entropy for optoelectronic applications, *Appl. Phys. A*, 2026, **132**(3), 176, DOI: 10.1007/s00339-026-09361-0.

49 S. Aydi, I. Garoui, S. Nasri, M. Akermi, R. Djebali and A. Oueslati, Engineering spinel ferrites *via* A-site cation Substitution: Structural, electrical, and optical properties for advanced applications, *Ceram. Int.*, 2025, **51**(26), 48861–48877, DOI: 10.1016/j.ceramint.2025.08.136.

50 D. Johnson, *ZPlot, ZView Electrochemical Impedance Software*, Version 2.3 b, Scribner Associates Inc., North Carolina, 2000.

51 M. Mnakri, I. Gharbi, M. Enneffati and A. Oueslati, Synthesis and investigation on the optical and complex impedance analysis in LiCrO2 prepared using solid-state reaction, *Mater. Today Commun.*, 2024, **38**, 107714, DOI: 10.1016/j.mtcomm.2023.107714.

52 M. Bharathi, S. Chapi, N. Nandihalli and M. V. Murugendrappa, Negative Temperature Coefficient of Resistance (NTCR) of Bismuth Manganite Nanoparticles: Polypyrrole Conductivity Enhancement, *J. Compos. Sci.*, 2025, **9**(5), 224, DOI: 10.3390/jcs9050224.

53 I. Khelifi, *et al.*, Comprehensive analysis of a novel iron(III) bromide based organic-inorganic hybrid material: Structural, conduction mechanisms and magnetic properties studies, *Mater. Today Commun.*, 2026, **51**, 114862, DOI: 10.1016/j.mtcomm.2026.114862.

54 M. Karray, I. Garoui, M. Akermi, R. Djebali, A. Oueslati and M. Gargouri, Implementing a solid-state synthesis route to tune the functional properties of NaCdP3O9 metaphosphate: optical characteristics, ionic conductivity, and dielectric behavior, *RSC Adv.*, 2025, **15**(36), 29703–29719, DOI: 10.1039/d5ra04138d.

55 O. Madkhali, Li2CaP2O7 pyrophosphate ceramics with dual functionality: high-performance NTC thermistor behavior and giant dielectric permittivity, *RSC Adv.*, 2026, **16**(21), 19457–19469, DOI: 10.1039/d6ra00134c.

56 S. Jagtap, S. Rane, S. Gosavi, U. Mulik and D. Amalnerkar, Infrared properties of 'lead free' thick film NTC thermo-resistive sensor based on the mixture of spinel material and RuO2, *Sens. Actuators, A*, 2013, **197**, 166–170, DOI: 10.1016/j.sna.2013.03.037.

57 Y. Q. Gao, *et al.*, Structural and electrical properties of Mn1.56Co0.96Ni0.48O4 NTC thermistor films, *J. Mater. Sci. Eng. B*, 2014, **185**, 74–78, DOI: 10.1016/j.mseb.2014.02.011.

58 S. Ben Yahya, I. Garoui, A. Oueslati and B. Louati, Structural, Optical, and Conduction Relaxation Properties of TlCrP2O7 Driven by Nonoverlapping Small Polaron Tunneling, *ACS Omega*, 2026, **11**(4), 6227–6240, DOI: 10.1021/acsomega.5c10392.

59 A. K. Jonscher, The 'universal' dielectric response, *Nature*, 1977, **267**(5613), 673–679, DOI: 10.1038/267673a0.

60 I. Garoui, M. Mallek, F. N. Almutairi, W. Rekik and A. Oueslati, Synthesis, Structural characterization and complex impedance analysis of a novel organic-inorganic hybrid compound based on Mercury(II) chloride, *J. Mol.*

Struct., 2024, **1315**, 138881, DOI: 10.1016/j.molstruc.2024.138881.

61 L. Dong *et al.*, "*Electrical Properties and Dielectric Relaxation Analysis of ZnAl2O4@ZnO Core–Shell Heterostructures*," Precision Chemistry, Jan. 2026, DOI: 10.1021/prechem.5c00196.

62 Y. Moualhi, *et al.*, Elaboration of La (Sr/Na) Mn (Ti) O3 ceramic, structural, and morphological investigations, and contribution of direct and indirect interactions on transport properties, *Ceram. Int.*, 2024, **50**(9), 16587–16597, DOI: 10.1016/j.ceramint.2024.02.149.

63 H. Elgahami, K. Ben Brahim, S. Hajlaoui, M. A. Alamri, G. Corbel and A. Oueslati, Synthesis and zero-dimensional structure of a new lead-free organic inorganic [(C2H5)4N] 3Bi2I9 compound: a promising material for optoelectronic devices, *RSC Adv.*, 2026, **16**(12), 10785–10797, DOI: 10.1039/d5ra09365a.

64 M. A. Fersi, R. Hajji, I. Chaabane and M. Gargouri, Synthesis, crystal structure and electrical properties of the new organic-inorganic hybrid compound bis(1-chlorido-4-aminopyridinium) octachlorodiantimoinate, *Phys. E*, 2017, **94**, 167–173, DOI: 10.1016/j.physe.2017.08.010.

65 S. R. Elliott, Temperature dependence of a.c. conductivity of chalcogenide glasses, *Philos. Mag. B*, 1978, **37**(5), 553–560, DOI: 10.1080/01418637808226448.

66 A. Ghosh and D. Chakravorty, AC conduction in semiconducting CuO-Bi2O3-P2O5glasses, *J. Phys.: Condens. Matter*, 1990, **2**(24), 5365–5372, DOI: 10.1088/0953-8984/2/24/009.

67 M. Mallek, I. Garoui, F. N. Almutairi, I. Chaabane, W. Rekik and A. Oueslati, Synthesis, structural characterization, Hirshfeld surface analysis, and electrical properties of a zinc (II)-based organic–inorganic hybrid compound, *J. Mater. Sci.: Mater. Electron.*, 2025, **36**(8), 458, DOI: 10.1007/s10854-025-14480-0.

68 S. Nasri, M. Megdiche and M. Gargouri, DC conductivity and study of AC electrical conduction mechanisms by non-overlapping small polaron tunneling model in LiFeP2O7 ceramic, *Ceram. Int.*, 2016, **42**(1), 943–951, DOI: 10.1016/j.ceramint.2015.09.023.